The Spectroscopic Classification of Astronomical Transients (SCAT) Survey:
Overview, Pipeline Description, Initial Results, and Future Plans

M. A. Tucker,[1,2,3,*] B. J. Shappee,[4] M. E. Huber,[4] A. V. Payne,[4] A. Do,[4] J. T. Hinkle,[4] T. de Jaeger,[4]
C. Ashall,[5] D. D. Desai,[4] W. B. Hoogendam,[4,†] G. Aldering,[6] K. Auchettl,[7,8,9] C. Baranec,[10] J. Bulger,[4]
K. Chambers,[4] M. Chun,[10] K. W. Hodapp,[10] T. B. Lowe,[4] L. McKay,[10] R. Rampy,[4] D. Rubin,[4] and J. L. Tonry[4]

[1]*Center for Cosmology and Astroparticle Physics, The Ohio State University, 191 West Woodruff Ave, Columbus, OH, USA*
[2]*Department of Astronomy, The Ohio State University, 140 West 18th Avenue, Columbus, OH, USA*
[3]*Department of Physics, The Ohio State University, 191 West Woodruff Ave, Columbus, OH, USA*
[4]*Institute for Astronomy, University of Hawai'i at Mānoa, 2680 Woodlawn Dr., Honolulu, HI, USA*
[5]*Department of Physics, Virginia Tech, Blacksburg, VA 24061, USA*
[6]*Lawrence Berkeley National Laboratory, One Cyclotron Rd., Berkeley, CA, 94720, USA*
[7]*School of Physics, The University of Melbourne, Parkville, VIC 3010, Australia*
[8]*ARC Centre of Excellence for All Sky Astrophysics in 3 Dimensions (ASTRO 3D)*
[9]*Department of Astronomy and Astrophysics, University of California, Santa Cruz, CA 95064, USA*
[10]*Institute for Astronomy, University of Hawai'i at Mānoa, Hilo, HI 96720, USA*

ABSTRACT

We present the Spectroscopic Classification of Astronomical Transients (SCAT) survey, which is dedicated to spectrophotometric observations of transient objects such as supernovae and tidal disruption events. SCAT uses the SuperNova Integral-Field Spectrograph (SNIFS) on the University of Hawai'i 2.2-meter (UH2.2m) telescope. SNIFS was designed specifically for accurate transient spectrophotometry, including absolute flux calibration and host-galaxy removal. We describe the data reduction and calibration pipeline including spectral extraction, telluric correction, atmospheric characterization, nightly photometricity, and spectrophotometric precision. We achieve $\lesssim 5\%$ spectrophotometry across the full optical wavelength range $(3500 - 9000$ Å$)$ under photometric conditions. The inclusion of photometry from the SNIFS multi-filter mosaic imager allows for decent spectrophotometric calibration $(10 - 20\%)$ even under unfavorable weather/atmospheric conditions. SCAT obtained ≈ 640 spectra of transients over the first 3 years of operations, including supernovae of all types, active galactic nuclei, cataclysmic variables, and rare transients such as superluminous supernovae and tidal disruption events. These observations will provide the community with benchmark spectrophotometry to constrain the next generation of hydrodynamic and radiative transfer models.

Keywords: Transient sources – spectrophotometry – supernovae – atmospheric extinction – active
galactic nuclei – cataclysmic variable stars

1. INTRODUCTION

The past decade in astronomy has seen a huge increase in the amount of observational data available to the community, largely due to the proliferation of imaging surveys. Some surveys, such as the All-Sky Automated Search for SuperNovae (ASAS-SN; Shappee et al. 2014; Kochanek et al. 2017) and the Asteroid Terrestrial-impact Last Alert System (ATLAS; Tonry et al. 2018a), cover the entire sky at moderate ($\lesssim 19$ mag) depth. Complementary surveys, such as the Panoramic Survey Telescope and Rapid Response System (Chambers et al. 2016, Pan-STARRS;), the Zwicky Transient Facility (ZTF; Bellm et al. 2019), and the upcoming Large Synoptic Survey Telescope (LSST; Ivezić et al. 2019),

Corresponding author: Michael Tucker
tuckerma95@gmail.com

[*] CCAPP Fellow
[†] NSF Graduate Research Fellow

provide or will provide deeper coverage for select portions of the sky.

Nearly every field of astronomy has benefited from the calibrated time-series photometry supplied by such surveys. However, these surveys have been particularly beneficial for studying astrophysical transients. These objects, such as supernovae (SNe) and tidal disruption events (TDEs), are stochastic events that provide fleeting glimpses into the physical processes governing extreme events in the Universe. In the past, a few hundred SNe were discovered per year by targeted galaxy surveys (e.g., Hamuy et al. 1993; Li et al. 2000; Aldering et al. 2002), but the current era of imaging surveys has increased the transient discovery rate hundred-fold (e.g., Kulkarni 2020). This deluge of discoveries has revealed both new types of transients, such as "fast blue optical transients" (FBOTs; e.g., Prentice et al. 2018; Ho et al. 2021), as well as extending our knowledge of rare and unique versions of known events, such as the faint SNe Iax class (e.g., Wood-Vasey et al. 2002; Li et al. 2003; Foley et al. 2013) of thermonuclear explosions.

While imaging surveys have undoubtedly transformed our understanding of the Universe and the myriad of explosive events that can occur within it, even well-sampled multi-filter photometry has its limitations. Spectroscopy is necessary for accurate transient classification and for constraining physical quantities such as temperature, density, and velocity which are essential for constructing a useful model. In addition to the program described in this manuscript, other notable transient classification programs include the ZTF Bright Transient Survey (BTS; Fremling et al. 2020; Perley et al. 2020) and the "advanced" extended Public ESO Spectroscopic Survey of Transient Objects (ePESSTO+, Smartt et al. 2015). Time-series spectroscopy, where multiple spectra are obtained over days or weeks, provides a view into how these quantities evolve with time, which, in turn, probes the underlying powering mechanism(s) (e.g., Ashall et al. 2014; Nicholl et al. 2014; Holoien et al. 2020; Dimitriadis et al. 2022).

However, most spectroscopic observations are obtained with slit spectrographs, where a finite-width slit is placed before the dispersive element in the optical path. The slit ensures stable spectral resolution and prevents contamination from other sources in the field of view (FoV) but makes absolute flux calibration[1] difficult. The amount of light passing through the slit depends on the slit alignment and the atmospheric seeing.

---

[1] When referencing absolute fluxes in this work, we are implicitly referring to the CALSPEC system (Bohlin et al. 2014) which provides absolute flux scalings accurate to $\approx 1\%$.

Additionally, atmospheric differential refraction (ADR) introduces a wavelength dependence on the amount of light passing through the slit (e.g., Filippenko 1982), especially for long exposures. This complicates the comparison between observations and physical models.

Spectrophotometry, where dispersed spectra are calibrated to an absolute flux scale, is *possible* for slit spectrographs in some cases. Time-series spectra combined with well-sampled high-quality photometry can produce decent spectrophotometric results by "mangling" or "warping" the observed spectra to match the photometry (e.g., Hsiao et al. 2007). However, this process is imperfect, especially for objects that do not have smooth spectral energy distributions due to strong absorption or emission features.

Integral field units (IFUs) or integral field spectrographs (IFSs) simultaneously disperse an entire FoV which is ideal for spectrophotometry of transients. Slit effects are no longer a concern, retaining absolute photometry capabilities, and observations of spectrophotometric standard stars ensure a reliable spectral shape. Additionally, most transients occur in external galaxies and require mitigation of coincident host-galaxy light. The combined spectral and spatial information provided by IFU observations is essential for accurate host-galaxy removal and, therefore, absolute calibration of the transient spectrum.

Here we describe the Spectroscopic Classification of Astronomical Transients (SCAT) survey which is dedicated to spectrophotometric observations of transient phenomena. §2 describes the survey motivation and facilities. Then, we outline the data reduction and calibration procedures in §3. §4 describes the necessary steps for placing the observed spectra on a reliable absolute flux scale. Finally, preliminary results and future developments are presented in §5.

2. SURVEY OVERVIEW

2.1. *Motivation*

The SCAT survey is designed to maximize the scientific return of imaging sky surveys. The science objectives are two-fold: publicly classify bright, nearby, and/or interesting transients, and initiate spectrophotometric follow-up for the most intriguing objects.

Classification targets are primarily selected based on brightness, and we impose a limiting magnitude of ≈ 19 mag (in optical filters) which provides a decent-quality extracted spectrum (S/N ~ 10) in ≈ 30 minutes under typical conditions (quarter moon, thin/cirrus clouds). After extracting the spectrum with a custom quick-reduction pipeline, all transient classifications are released to the public via the Transient Name Server

(TNS)[2]. We caution that the quick-reduction pipeline does not ensure absolute flux calibration (see §5.1).

Spectrophotometric follow-up observations are obtained for particularly interesting transient sources. Follow-up targets generally fall into two categories: bright or unique. Bright transients are ideal for obtaining well-sampled high-quality spectrophotometry with the purpose of testing our understanding of the physical processes involved. Unique transients offer a different view into transient phenomena, as these sources are often poorly characterized and any data is useful to the community as we strive to constrain the mechanism(s) governing their formation and evolution. A subset of recent results using SCAT data is described in §5.

2.2. *Telescope and Instrumentation*

The SCAT survey utilizes the SuperNova Integral Field Spectrograph (SNIFS; Lantz et al. 2004) on the University of Hawai'i 2.2 m (UH2.2m) telescope. SNIFS was built by the Nearby Supernova Factory (SNfactory; Aldering et al. 2002), and expressly designed to deliver transient spectrophotometry. SNIFS is comprised of three components: the photometric P channel and the two spectroscopic (B+R) channels.

The P channel is responsible for acquiring, imaging, and guiding. The current filter set includes SDSS *ugriz* plus Bessel *V*-band and the multi-filter (MF) mosaic, described below. Each image covers $9' \times 9'$ with a pixel scale of $0\rlap{.}{''}137$ per pixel. The full-frame image is comprised of 2 CCDs with a 77-pixel ($\approx 10''$) vertical chip gap in the center. Under typical conditions, a 20 s *V*-band acquisition image has a limiting magnitude of $V \approx 19$ mag. A unique component of the SNIFS P channel is the inclusion of the MF imaging setup comprised of 5 custom filters shown in Fig. 1. The filters are designed to probe different aspects of the atmospheric throughput (Buton 2009).

Light is sent to the spectroscopic B and R channels using a pick-off prism (POP). After deflection by the POP, incident light is split between the B and R channels with a dichroic mirror then sent to the microlens arrays, each having a $6'' \times 6''$ FoV. The B channel covers $\approx 3400 - 5100$Å and the R channel covers $\approx 5100 - 10000$ Å, providing complete spectroscopic coverage across the full optical range. The spectral resolutions of the B and R channels are ≈ 5 Å and ≈ 7 Å, respectively.
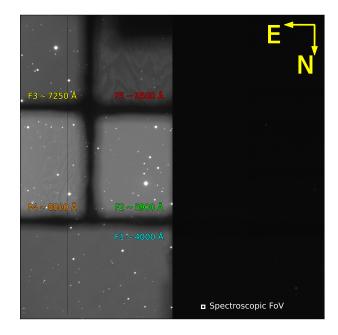

Figure 1. Example image of the multi-filter (MF) mosaic with effective wavelengths marked for each filter. The lower-right white square represents the $6'' \times 6''$ FoV of the spectroscopic channels.

3. SCAT DATA REDUCTION AND CALIBRATION

The performance of the SNIFS+UH2.2m optical system has been extensively tested and calibrated by the SNfactory team (Aldering et al. 2002). SNfactory is dedicated to time-series spectrophotometry of Type Ia supernovae (SNe Ia) for measuring cosmological parameters. To achieve this goal, they have calibrated the SNIFS spectrophotometric response to within 0.3% of the Hubble Space Telescope (HST) CALSPEC system (Rubin et al. 2022), the de facto "gold standard" in spectrophotometry (Bohlin et al. 2014). SNfactory is able to reach this level of precision by dedicating a significant amount of time and effort to calibrating each aspect of the optical system, including extensive standard-star observations (e.g., Buton et al. 2013) and the implementation of the SNIFS Calibration Apparatus (SCALA; Küsters et al. 2016; Lombardo et al. 2017; Küsters et al. 2020). Additionally, the SNfactory data reduction pipeline includes several algorithms that are not implemented in our pipeline. These corrections, such as the binary offset effect in CCD images (Boone et al. 2018), mitigate sources of noise below our desired threshold.

As outlined in §2, our goal is distinct from that of the SNfactory team. SCAT observes transients for understanding the physical processes governing the transient phenomena that occur throughout the Universe. We prioritize integration time on science targets by obtaining
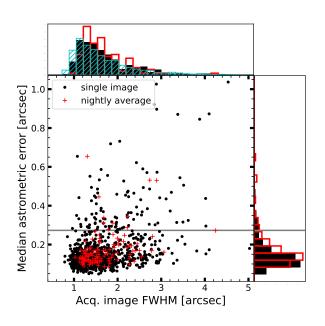
Figure 2. Comparison of the acquisition image FWHM to the median astrometric error. Black and red points represent single-exposure and nightly averaged values, respectively. The blue hatched histogram along the top shows the guider FWHM measurements from Fig. 3. Acquisition images are obtained with 2×2 binning resulting in a pixel scale of $0.''27$/pixel (grey horizontal line).
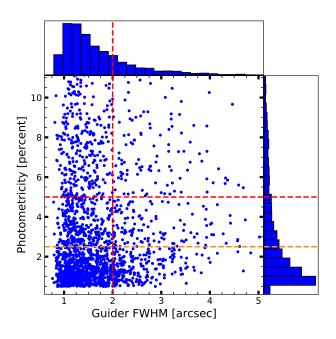

Figure 3. Comparison of the guider FWHM to the photometricity. Dashed lines represent the thresholds for photometric (orange) and non-photometric (red) conditions (see §4.2).

minimal calibration data throughout the night. Here we detail the photometric data reduction process in §3.1 and the spectroscopic procedure in §3.2. This section draws extensively from Da Silva Pereira (2008) and Buton (2009) which laid the groundwork for the absolute calibration of SNIFS observations.

3.1. *P Channel*

The P-channel images are overscan and dark subtracted, then flat-fielded using a median-combined sky flat constructed from 200 randomly-selected exposures taken during adjacent observing nights, with a maximum allowable time difference of 2 weeks. Exposures with short integration times (< 5 s) are excluded to avoid bright ($V \sim 6$ mag) standard stars. Finally, the astrometric solution is derived using the Astrometry.net software package (Lang et al. 2010). Fig. 2 compares the median astrometric error, measured as the offset between the reference coordinates and the coordinates derived from the source positions, to the image FWHM. The majority of acquisition images have sub-pixel astrometric precision.

During spectroscopic exposures, stars that fall in the SNIFS P-channel FoV are imaged concurrently through one of the available filters, usually the MF or V-band

filter. The MF images cannot be astrometrically calibrated with the Astrometry.net software due to the inter-filter gaps and the low number of reference stars. Instead, we use the telescope offset between the V-band acquisition image and the MF image to obtain a coarse alignment which is then tweaked (up to a few arcseconds) by centroiding stars detected in both frames.

After astrometric calibration, we perform PSF-fitting photometry on each image. The full-frame V-band acquisition images have enough stars where the PSF can be derived independently for each image. For the MF images, we apply the wavelength-dependent PSF fit from the spectroscopic exposure (see §3.2) because the spectroscopic and photometric PSFs are similar (Da Silva Pereira 2008). Finally, we zeropoint each image using the REFCAT catalog (Tonry et al. 2018b). Stars used to model the PSF are required to have no sources within $5''$ and $12 < m$ [mag] < 18. The brightness and crowding limitations are removed when applying the PSF to sources detected in the image except for the exclusion of saturated objects. Sources that are separated by $< 2 \times$ FWHM have their PSF fluxes fit simultaneously with a common background level.

3.2. *B and R channels*

The overall spectroscopic reduction process is similar for both B and R channels. The 2D spectroscopic exposures are pre-processed by the UH2.2m summit comput-
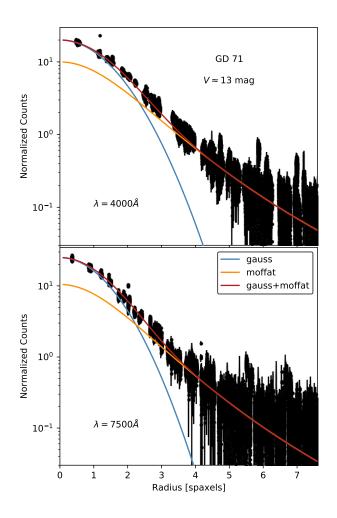
Figure 4. Example PSF fits to the B (top) and R (bottom) channels for a faint spectrophotometric standard star, GD71, including the Gaussian core (blue), the Moffat wings (orange), and the total PSF (red).

ers including bias and overscan subtraction, bad pixel masking, wavelength calibration with arc-lamp exposures, and finally converted into 3D (x, y, λ) datacubes (Bacon et al. 2001). Then, the extracted datacubes are transferred to our data reduction server. The datacubes are flat-fielded with nightly continuum lamp exposures and cosmic-ray hits are detected and interpolated over. Then, the extraction trace and ellipticity are estimated by fitting a wavelength-dependent 2D Gaussian profile to "meta-slices" with widths of 100 Å and 150 Å for the B and R channels, respectively. Then, we construct the normalized radial PSF which is well-described by a Gaussian core and Moffat wings (Buton 2009; Rubin et al. 2022);

$$PSF(r_e, \sigma, \eta, \alpha, \gamma) = \eta \times G(r_e, \sigma) + M(r_e, \alpha, \gamma) \quad (1)$$
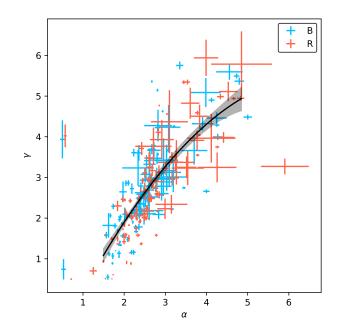

Figure 5. Correlation between the Moffat power-law index α and the radial term γ for the central wavelengths of the B and R channels. The black line represents a quadratic fit to the combined data with the shaded region signifying the uncertainty. Fitting each channel separately produces a correlation in agreement with the fit to the combined data to better than 0.5σ.

where $G(r)$ describes the Gaussian core with standard deviation σ, $M(r)$ represents the Moffat wings with radial scale term γ and power-law index α, and η determines the contribution from each component. The PSF may not be exactly circular, usually due to small guiding errors and slight atmospheric distortions, so we compute the elliptical radius

$$r_e^2 = (x - x_0)^2 + A(y - y_0)^2 + 2B(x - x_0)(y - y_0) \quad (2)$$

where (x_0, y_0) represent the center of the PSF and the ellipticity is described by the parameters A and B.

Standard-star spectra are extracted by fitting

$$F_\lambda = I_\lambda \times PSF(r_e, \sigma, \eta, \alpha, \gamma) + c_\lambda \quad (3)$$

to the 3D cube using a Markov Chain Monte Carlo (MCMC) sampler with a χ^2 minimization loss function and uninformative priors on the parameters. The observed flux F_λ is comprised of the incident source flux, I_λ, modulated by the PSF (Eq. 1) and the addition of a spatially uniform background c_λ. We build a PSF template library using the standard-star spectra with "good" PSF fits (i.e., $\chi^2/\nu \sim 1$) to measure parameter correlations and wavelength dependencies.
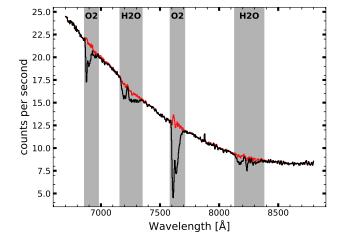
Figure 6. A randomly-selected standard-star spectrum before (black) and after (red) correcting for telluric absorption.

These parameter correlations are used as informative priors when extracting science exposures. Fig. 5 shows that the Moffat parameters α and γ can be tied during the fitting process and we use the fitted correlation (the black line in Fig. 5) as a Gaussian prior at each λ. Additionally, the Gaussian FWHM is set to the guide star FWHM at $\lambda \approx 5500$ Å (i.e., V-band). This reduces the number of variables in the PSF fit to just 2, and therefore only 4 free parameters in Eq. 3: I_λ, c_λ, η, and a joint parameter representing the Moffat α and γ terms.

4. SPECTROPHOTOMETRY AND ABSOLUTE FLUX CALIBRATION

SNIFS was designed for transient spectrophotometry (Aldering et al. 2002) but several steps are necessary to ensure the nightly flux calibration is accurate. We present our atmospheric model in §4.1, outline the criteria for photometric conditions in §4.2, and describe the procedure for deriving the nightly atmospheric and flux solutions in §4.3.

4.1. Atmospheric Transmission

Spectra must be corrected for atmospheric extinction in order to be placed on a reliable absolute flux scale. Following Buton et al. (2013), the total atmospheric extinction (excluding telluric lines) is comprised of three components: Rayleigh scattering, aerosol scattering, and ozone absorption. The Rayleigh component is essentially non-variable (Buton et al. 2013), leaving three free parameters describing the two remaining components. The ozone template is multiplied by a dimensionless scale factor corresponding to the strength of the absorption features at < 3300 Å and $5000-7000$ Å. The

aerosol component is parameterized as a power-law with 2 free parameters (e.g., Reimann et al. 1992),

$$k_A(\lambda) = \tau_1 \times (\lambda/1 \ \mu\mathrm{m})^{-\mathring{a}} \qquad (4)$$

with inverse wavelength exponent $\mathring{a}$ and 1μm optical depth τ_1.

Gaussian priors on the atmospheric parameters are similar to those adopted by Buton et al. (2013), namely $\mathring{a} = 1\pm3$ and $\log_{10}\tau_1 = -2\pm1$. The O_3 absorption template we generate with molecfit (Smette et al. 2015; Kausch et al. 2015) is similar, but not identical, to the template used by Buton et al. (2013). Our ozone template is normalized such that median conditions on Maunakea produce a scale factor of 1 and we adopt the same (fractional) uncertainty as Buton et al. (2013) of 20%.

4.2. Nightly Photometricity

The photometric stability (i.e., photometricity) of each night must be assessed to determine the reliability of the flux solution. Several probes are used in conjunction to determine if a given night is photometric. Table 1 provides a summary of the criteria which we elaborate upon here.

SkyProbe: The SkyProbe atmospheric monitor (Cuillandre et al. 2002; Steinbring et al. 2009; Cuillandre et al. 2016) is part of the Canada-France-Hawai'i Telescope (CFHT) and is dedicated to real-time measurements of the atmospheric transmission. As outlined in Buton et al. (2013), some cleaning of the raw SkyProbe transmission measurements is necessary to eliminate spurious points and correct inter-pointing offsets. After processing, transmission RMS values of $\leq 2.5\%$ indicate excellent conditions and $> 5\%$ RMS indicate poor conditions.

Quality of the PSF fit: How well the PSF is fit by the model (Eq. 1) is another avenue for constraining the photometricity of a given exposure. Poorly-modeled PSFs can be attributed to several different aspects of the observing and atmospheric conditions. For example, large and/or highly variable seeing make it difficult to precisely measure the PSF shape parameters because of the trade-offs between the Gaussian core, the Moffat wings, and the background sky flux. No exposure with a seeing of $> 2''$ is considered photometric, as Rubin et al. (2022) showed the PSF becomes poorly behaved under these conditions. Other factors that can degrade the quality of the PSF fit include imprecise focusing or telescope jitter caused by wind shake. Empirically, reduced chi-squared statistics of $\chi^2/\nu > 1.5$ represent a poor fit to the data and thus unlikely to be photometric and PSF fits with $\chi^2/\nu \leq 1.2$ are considered photometric.

Photometric Zeropoints: The uncertainty on the derived photometric zero points constrains the stability of

Probe	Photometric	Non-photometric
Single Exposure Criteria		
PSF fit χ^2/ν	≤ 1.2	> 1.5
Guide star flux RMS	$\leq 2.5\%$	$> 5\%$
Nightly Criteria		
SkyProbe Transmission RMS	$\leq 2.5\%$	$> 5\%$
Median Seeing	$< 1.5''$	$> 2''$
V-band zeropoint uncert.	≤ 0.03 mag	> 0.05 mag
MF zeropoint uncert.	≤ 0.05 mag	> 0.1 mag
Standard-star flux solution RMS	$\leq 3\%$	$> 5\%$
Photometric exposure fraction	1	< 0.75

Table 1. Criteria used when determining the photometricity of a given observing night. Photometric nights have stable atmospheric conditions and negligible cloud extinction, ideal conditions for spectrophotometry. Non-photometric nights have unstable/turbulent atmosphere and/or detectable cloud cover. The intermediate classification, semi-photometric nights, do not exceed any of the non-photometric thresholds but also do not meet all of the photometric criteria.

the atmosphere over the course of the night, as non-photometric conditions will introduce intrinsic scatter into the nightly photometry. We use different thresholds for the V-band acquisition images and the MF filters because there is typically an order of magnitude or more stars available for the V-band observations. Therefore, the V-band solution has typical uncertainties $\lesssim 0.01$ mag whereas the MF zeropoint uncertainties are typically $\sim 0.02 - 0.06$ mag.

Flux solution: The RMS of the derived flux calibration is a measure of how well the observed standard-star spectra are reproduced by our atmospheric and instrumental solutions. SNIFS has a single-exposure extraction floor of a few percent (Buton 2009; Rubin et al. 2022) so we set an upper limit on the flux calibration RMS of 3% for photometric conditions. The non-photometric regime is characterized by standard-star RMS in excess of 5%, our desired spectrophotometric accuracy.

Photometric exposure fraction: The photometric exposure fraction is determined by comparing the number of exposures that meet the single-exposure photometric criteria, namely the RMS of the guide-star flux and the measured seeing, to the total number of exposures obtained that night. All exposures must be photometric for a given night to be considered photometric and nights with $< 75\%$ of exposures meeting the photometric criteria are considered non-photometric because the aerosol component of the atmospheric model can compensate for persistent low-extinction cloud cover (c.f. Fig. 13 from Buton et al. 2013). Bright ($V \approx 6$ mag) standard-star observations are excluded when calculating the photometric exposure fraction because the short exposure times (≈ 1 s) can produce aberrant PSF shapes even under good conditions.

Combining the criteria outlined above and in Table 1, we can assess the photometricity of a given night.

The photometric criteria are restrictive by design so all photometric criteria must be met for a given night to be considered photometric. Similarly, a night meeting or exceeding any of the non-photometric criteria are deemed non-photometric. The intermediate classification, semi-photometric nights, occurs when none of the non-photometric criteria are met, but neither are all of the photometric criteria. These nights usually are affected by passing and/or thin clouds that only affect some of the exposures. For these nights, photometricity is handled on a "rolling" basis where the longest uninterrupted time-span of exposures meeting the photometric criteria is considered photometric, and the remaining time is non-photometric. This relies mostly on the photometric exposure fraction, as no more than 25% of the exposures can be considered non-photometric to ensure that a reliable atmospheric and flux solution can still be derived.

Note that the concurrent V-band or MF images provide spectrophotometric capabilities even under non-photometric conditions but with a significantly higher uncertainty ($\sim 10 - 20\%$) compared to photometric conditions ($\leq 5\%$) due to the limited number of calibration stars in the P-channel FoV. A full description and analysis of the long-term spectrophotometric accuracy, including uncertainty estimation for non-photometric conditions, will be presented in a forthcoming paper.

4.3. *Deriving the nightly atmospheric and flux solution*

We utilize both photometry and spectroscopy to derive each night's atmospheric parameters. First, we leverage the P-channel photometry to derive broadband wavelength-dependent extinction coefficients. We typically obtain ≥ 15 V-band acquisition images and $5 - 7$
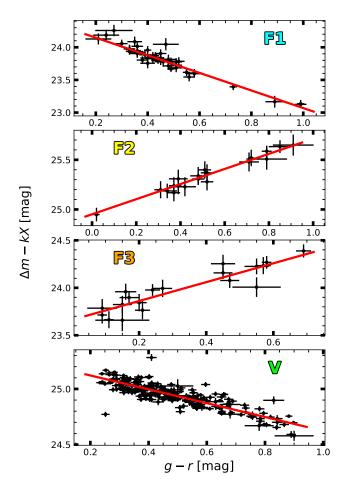
Figure 7. Results from fitting the photometric coefficients (Eq. 5) to photometry from the V-band acquisition images and the $F1$, $F2$, and $F3$ filters. The fitted coefficients for each filter provided in Table 2 constrain the atmospheric transmission (see §4.1) and the nightly photometricity (see §4.2). Note that airmass corrections have been applied.

Filter	z	t	k
	[mag]		[mag/airmass]
$F1$	24.42 ± 0.03	-1.35 ± 0.05	0.27 ± 0.02
$F2$	24.95 ± 0.04	0.76 ± 0.03	0.14 ± 0.04
$F3$	23.66 ± 0.05	0.99 ± 0.07	0.06 ± 0.04
V	25.25 ± 0.01	-0.62 ± 0.01	0.11 ± 0.01

Table 2. Filter coefficients from Eq. 5 for the data shown in Fig. 7 and the top panel of Fig 8.

MF images during a typical observing night. The equation

$$m_{\rm ref} - m_{\rm obs} = \Delta m = z + t(g - r) + kX \qquad (5)$$

converts the observed instrumental magnitude, $m_{\rm obs}$, into the reference filter magnitude $m_{\rm ref}$ at airmass X using the zeropoint z, atmospheric extinction coefficient k, and color coefficient t corresponding to the $g - r$ color from REFCAT (Tonry et al. 2018b). Only the $F1$ ($\lambda_{\rm eff} \approx 4000$ Å), $F2$ ($\lambda_{\rm eff} \approx 5900$ Å), and $F3$ ($\lambda_{\rm eff} \approx 7250$ Å) filters are used from the MF mosaic due to the redder $F4$ and $F5$ filters being contaminated by the strong H_2O absorption from $\sim 0.9 - 1$ μm. Fig. 7 shows example results from fitting Eq. 5 to each set of filter photometry with the coefficients provided in Table 2.

Then, the observed spectra are corrected for molecular absorption bands caused by O_2 and H_2O. We start with a high-resolution absorption template generated using MOLECFIT (Smette et al. 2015; Kausch et al. 2015). These absorption bands are typically saturated and follow an airmass dependence of $k_\oplus = sX^\rho$, with ρ representing the saturation parameter, X is the exposure's airmass, and s is a dimensionless scale factor. We adopt a non-variable $\rho_{\rm O2} = 0.6$ as this has been shown to produce excellent results for Maunakea (Buton et al. 2013). The H_2O saturation parameter $\rho_{\rm H2O}$ is also fixed to 0.6 if fewer than 5 standard-star observations are available, otherwise $\rho_{\rm H2O}$ is allowed to vary. We include an additional free parameter that convolves the high-resolution absorption template to account for minor wavelength differences between the spectra and the MOLECFIT model. An example telluric correction is shown in Fig. 6. We do not attempt to correct for the H_2O absorption band at > 9000Å because the continuum level is uncertain.

Finally, we use the telluric-corrected standard-star spectra to jointly fit the atmospheric extinction and the flux calibration solution. Table 1 in Rubin et al. (2022) lists the spectrophotometric standard-star targets observed with SNIFS. After binning the spectra into "meta-slices" (see §3.2), we fit

$$S_\lambda = \bar{S}_\lambda \times k_\lambda(X) \times T_\lambda \qquad (6)$$

with observed spectrum S_λ, the corresponding reference spectrum $\bar{S}_\lambda$, total atmospheric extinction k_λ at wavelength λ, and the combined instrumental and telescopic response T_λ modeled using a low-order spline. Buton et al. (2013) show that T_λ is a smoothly-varying function of wavelength on scales less than the meta-slice width (100 Å for the B-channel, 150 Å for the R-channel).

On photometric nights, the atmosphere is considered non-variable and cloud extinction is negligible, allowing direct calculation of k_λ and T_λ using the observed standard-star spectra. However, a different approach must be adopted for non-photometric conditions where
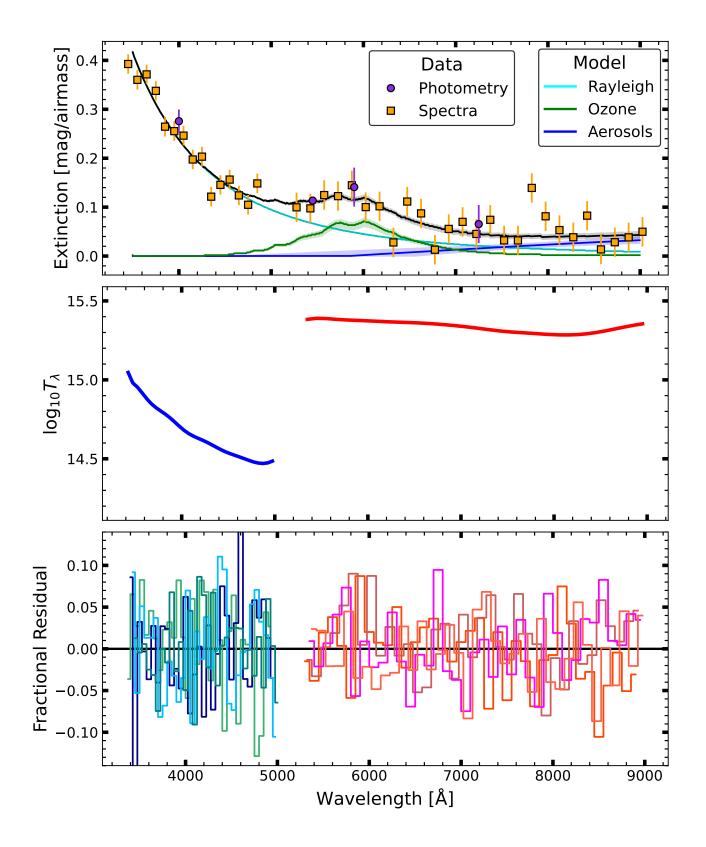
Figure 8. Example atmospheric and flux calibration solution for a typical night, UT 2020-02-15. *Top*: Atmospheric extinction curve derived by jointly fitting the photometry (purple circles, see Fig. 7) and the standard-star spectra (orange squares). *Middle*: Derived flux-calibration curve for the night. Note that the normalized spectral flat field has been applied. *Bottom*: Per-spectrum residuals from our flux calibration pipeline for the 4 standard-star spectra. Individual spectra are arbitrarily offset along the x-axis for visual clarity.

thin and/or intermittent clouds can diminish the observed flux. On these nights, each standard-star observation is allowed to have non-zero cloud cover, parameterized as a grey (wavelength-independent) extinction component[3], that diminishes the observed flux by a factor of f. We require $0 < f < 1$ and use the corresponding MF or V-band photometry, if available, to place an additional prior on cloud cover during the exposure with a typical uncertainty of $\delta f/f \sim 10\%$. If < 3 standard-star observations are obtained for a given night, usually due to unfavorable weather conditions, we adopt the mean atmospheric extinction from Buton et al. (2013).

Example results of the atmospheric and flux calibration routines are shown for a typical photometric night, UT 2020-02-15, where 4 standard-star observations were obtained. The telluric correction for a randomly-selected standard-star spectrum is shown in Fig. 6, results from fitting Eq. 5 to the photometry are provided in Fig. 7, and Fig. 8 shows the derived atmospheric extinction curve, including its decomposition into the various physical components, and the derived flux calibration solution. The bottom panel of Fig. 8 shows the per-spectrum B-channel and R-channel residuals.

5. INITIAL RESULTS

Over the course of the 2018B−2020B observing semesters (i.e., UT 2018-02-01 through 2021-01-31), we obtained 635 science exposures over 101 nights[4]. Roughly 75% of the observations were dedicated to classifying transients and the remaining $\sim 25\%$ are follow-up observations. We provide details on classifications and follow-up observations in §5.1 and §5.2, respectively. §5.3 describes our data policy, and future plans for the SCAT survey are detailed in §5.4.

5.1. *Transient Classification*

The classification spectra are extracted with a quick-reduction pipeline which is very similar to the one described in §3 with two notable differences: 1) spectra are extracted using aperture photometry instead of PSF fitting, 2) the flux solution is relative instead of absolute, and 3) no effort is made to correct the dichroic crossover region. Extracting the spectra using aperture photometry instead of PSF fitting expedites the reduction process, allowing us to classify objects during the course of a
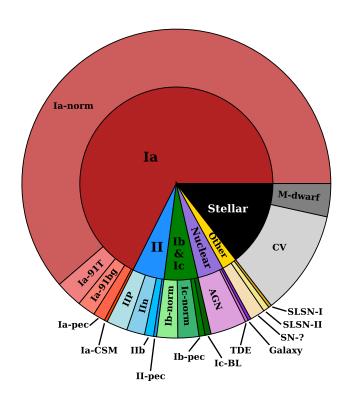
[3] Buton et al. (2013) showed that the chromaticity of cloud extinction is < 1%.

[4] Excluding nights where no observations were taken due to weather, maintenance, or COVID-related closures.

Figure 9. Distribution of transient classification types from the first 3 years of the SCAT survey.

night, but incurs drawbacks such as poorer host-galaxy subtraction. Similarly, adopting a relative flux solution allows the use of observations from other observing nights to construct the flux solution and avoid deriving a nightly atmospheric solution. Thus, classification spectra released via TNS are not guaranteed to have reliable absolute flux calibration and should not be used for such purposes without proper vetting. The dichroic, which deflects light between the B and R spectroscopic channels, has humidity-dependent transmission due to the use of a water-based coating. Special spectroscopic flat field images are taken before each science exposure to mitigate dichroic transmission variations but these spectral flats are not currently applied by the quick-reduction pipeline. Thus, the $\approx 5000 - 5200$ Å region should be treated with caution when analyzing classification spectra.

Transient spectra are classified via visual inspection with assistance from the SuperNova Identification (SNID) software (Blondin & Tonry 2007). Fig. 9 shows the different types of transients classified during the first 3 years of SCAT. 482 of the 635 exposures (75.9%)

were obtained for classification purposes, of which 369[5] ($\approx 75\%$) were classified and publicly released through TNS. Another $\approx 15\%$ of the classification targets were first classified by another transient classification program such as ePESSTO+ (Smartt et al. 2015) or the ZTF BTS (Fremling et al. 2020; Perley et al. 2020). The remaining $\sim 10\%$ of the exposures had a too-low signal for conclusive typing, usually obtained during unfavorable weather conditions.

5.2. Follow-Up Targets

The remaining $\approx 25\%$ of our observing time is reserved for extensive follow-up observations of interesting and unique discoveries from the world's sky surveys. Each follow-up target is typically observed several times over the course of the follow-up campaign which can span one or multiple semesters. While some of the follow-up spectra are still being analyzed, several papers have already been published using SCAT spectra on a variety of transient phenomena.

Many of the papers published using SCAT observations focus on TDEs. We classified PS18kh as a TDE during our first observing night in March 2018 (Tucker et al. 2018a) and initiated an extensive follow-up campaign leading to the first discovery of a TDE with an asymmetric accretion disk (Holoien et al. 2019). Other TDEs with SCAT spectra include ASASSN-19dj (Hinkle et al. 2021a), ASASSN-20hx (Hinkle et al. 2021b), and ATLAS18mlw (Hinkle et al. 2022a). It is unclear if ASASSN-18jd is a TDE or related to AGN activity (Neustadt et al. 2020), part of the growing number of Ambiguous Nuclear Transients (ANTs; e.g., Trakhtenbrot et al. 2019; Hinkle et al. 2022b).

Additionally, we have observed several other transients involving the interplay between black holes and their accretion environments including the low-mass X-ray binary (LMXB) ASASSN-18ey/MAXI J1820+070 (Tucker et al. 2018b) and the changing-look blazar B2 1402+32 (Mishra et al. 2021). Finally, we have also observed the young stellar object (YSO) outburst Gaia 19bey (Hodapp et al. 2020) and the intriguing SN Icn 2021csp (Fraser et al. 2021), part of the emerging class of SNe Ic with narrow C/O emission lines (e.g., Gal-Yam et al. 2022; Pellegrino et al. 2022). Many more papers are in various stages of analysis and publication, and this number will begin to increase dramatically due to our partnerships with the Hawai'i Supernova Flows

(HSF, Do et al., in prep) and the Precision Observations of Infant Supernovae (POISE; Burns et al. 2021) collaborations.

5.3. Data Policy and Releases

All spectra used to classify transients are made publicly available to the community through the TNS website. However, as noted in §5.1, the classification spectra are reduced with a simplified version of the reduction pipeline and are not guaranteed to have absolute spectrophotometry. Anyone wishing to obtain spectrophotometric-quality classification spectra should contact the SCAT team.

We plan on periodic data releases for the spectrophotometric observations. The precision spectrophotometry of our SCAT observations will be essential to test and constrain the next generation of physical models for a vast array of transient phenomena.

5.4. Future Plans

SCAT will benefit from several upgrades to the UH2.2m/SNIFS system over the next few months. The tertiary mirror was replaced in early 2022 which provides an increase in the total system throughput and allows observers to quickly switch between instruments. This capability is especially useful for STACam, a wide-field imager ($14.5' \times 14.5'$ FoV at $0.''08$/pixel) equipped with $grizy$ filters. Rapid switches between SNIFS and STACam provide contemporaneous imaging capabilities during the readout of the SNIFS CCDs. Thus, we can obtain improved multi-color photometry of transients and additional constraints on the atmospheric extinction (e.g., Figs. 7 and 8) with no additional observing time required.

Another instrument recently added to the UH 2.2-m is Robo-AO-2 (Baranec et al. 2018, 2021), an optical and near-infrared laser adaptive optics imaging system that provides spatial resolution approaching that of the Hubble Space Telescope. While the previous generation Robo-AO system (Baranec et al. 2014) was typically used for searching for companions to stellar and planetary systems (e.g., Ziegler et al. 2018; Lamman et al. 2020; Salama et al. 2021), SCAT will use the improved high-acuity imaging capabilities of Robo-AO-2 to quickly assess if transients close to the center of their host galaxies are truly nuclear, as with AGN variability and TDEs, or non-nuclear with a small projected separation.

Additionally, work is underway to make the UH2.2m system entirely robotic so no human intervention is necessary for nightly observations (Shappee et al., in prep). Observations will be scheduled automatically based on

---

[5] The best way to reproduce our numbers through the TNS web query is to use the following input values: 'Discovery Date Range' = (2018-02-01, 2021-01-31), Classification Instrument = 'UH88 - SNIFS', and check the 'Official Classification' box (link).

the score assigned by the telescope allocation committee. This will increase the amount of time spent on science targets because calibration data, mainly standard-star spectra, can be reserved for non-ideal weather conditions or nights with high moon illumination. Robotic operations also open many avenues for improving the per-night efficiency and expanding the capabilities of SCAT for observing rare and/or fast-declining transients.

Science data from LSST is expected in mid-2024[6] and subsequently, the number of transients discovered in the southern hemisphere is expected to increase drastically. The UH2.2m, located on Maunakea at a latitude of ≈ 19 deg, can observe objects with declination $\delta \gtrsim -40$ deg. As such, there will be significant overlap between UH2.2m's observable sky area and the LSST footprint ($\delta \lesssim +30$ deg). While most transients discovered by LSST will be too faint for classification with SNIFS, SCAT will observe some of these discoveries as they rise to peak brightness and allow larger-aperture telescopes to focus their time on fainter targets.

Starting in 2023, SCAT will also have access to the Wide-Field Spectrograph (WiFeS; Dopita et al. 2007) on the Australian National University 2.3-meter (ANU2.3m) telescope. There are many similarities between WiFeS+ANU2.3m and SNIFS+UH2.2m. Both are integral-field spectrographs on moderate-aperture telescopes covering the full optical wavelength range. WiFeS has a larger FoV ($25'' \times 38''$) and slightly higher spectral resolution ($R \sim 3000$). Incorporating WiFeS+ANU2.3m will improve our southern hemisphere capabilities where transients are already discovered by the ASAS-SN and ATLAS sky surveys, in addition to the upcoming LSST. Thus, SCAT will be able to obtain spectrophotometry of any $\lesssim 19$ mag transient regardless of sky position or discovery survey.

Multi-messenger synergy is an exciting avenue for future expansion, especially considering the upcoming improvements to SNIFS+UH2.2m and the inclusion of WiFeS+ANU2.3m. The astronomical community still lacks an understanding of which events detected via gravitational waves (e.g., LIGO/VIRGO, Aasi et al. 2015; Acernese et al. 2015; Abbott et al. 2021) or neutrinos (e.g., IceCube, Aartsen et al. 2013) will have optical counterparts. The sky localizations of these events usually span $\sim 10^2 - 10^3$ square degrees (Abbott et al. 2020) leading to many potential optical counterparts (e.g., Coughlin 2020; de Jaeger et al. 2022; Necker et al. 2022). These counterparts require spectroscopic confirmation to separate the multi-messenger sources from typical op-

tical transients such as SNe. However, early identification and follow-up of multi-messenger sources provides unprecedented insight into the physical processes governing these extreme events (e.g., Coulter et al. 2017; Shappee et al. 2017; Valenti et al. 2017; IceCube Collaboration et al. 2018; Garrappa et al. 2019). Robotic triggering of SNIFS will provide rapid follow-up capabilities for observing the extreme events in our Universe. Additionally, SNIFS readily provides precise spectrophotometric calibration whereas target-of-opportunity observations rarely contain the necessary calibrations for absolute spectrophotometry.

The proliferation of sky surveys has made it an exciting time for studying and understanding astrophysical transients. SCAT is specifically designed to capitalize on this discovery deluge and will provide the community with precise spectrophotometry necessary for testing the next generation of theoretical models.

SOFTWARE

numpy (Harris et al. 2020), astropy (Astropy Collaboration et al. 2013), lmfit (Newville et al. 2021), emcee (Foreman-Mackey et al. 2013), spectres (Carnall 2017), matplotlib (Hunter 2007), photutils (Bradley et al. 2019), scipy (Virtanen et al. 2020), pandas (Reback et al. 2022), astroscrappy (McCully et al. 2018)

FACILITIES

Facility: UH: 2.2m

ACKNOWLEDGEMENTS

REFERENCES

Aartsen, M. G., Abbasi, R., Abdou, Y., et al. 2013, PhRvL, 111, 021103, doi: 10.1103/PhysRevLett.111.021103

Aasi, J., Abadie, J., Abbott, B. P., et al. 2015, Classical and Quantum Gravity, 32, 115012, doi: 10.1088/0264-9381/32/11/115012

Abbott, B. P., Abbott, R., Abbott, T. D., et al. 2020, Living Reviews in Relativity, 23, 3, doi: 10.1007/s41114-020-00026-9

Abbott, R., Abbott, T. D., Abraham, S., et al. 2021, Physical Review X, 11, 021053, doi: 10.1103/PhysRevX.11.021053

Acernese, F., Agathos, M., Agatsuma, K., et al. 2015, Classical and Quantum Gravity, 32, 024001, doi: 10.1088/0264-9381/32/2/024001

Aldering, G., Adam, G., Antilogus, P., et al. 2002, in Society of Photo-Optical Instrumentation Engineers (SPIE) Conference Series, Vol. 4836, Survey and Other Telescope Technologies and Discoveries, ed. J. A. Tyson & S. Wolff, 61–72, doi: 10.1117/12.458107

Ashall, C., Mazzali, P., Bersier, D., et al. 2014, MNRAS, 445, 4427, doi: 10.1093/mnras/stu1995

Astropy Collaboration, Robitaille, T. P., Tollerud, E. J., et al. 2013, A&A, 558, A33, doi: 10.1051/0004-6361/201322068

Bacon, R., Copin, Y., Monnet, G., et al. 2001, MNRAS, 326, 23, doi: 10.1046/j.1365-8711.2001.04612.x

Baranec, C., Riddle, R., & Law, N. M. 2021, in The WSPC Handbook of Astronomical Instrumentation, Volume 2: UV, Optical & IR Instrumentation: Part 1, ed. A. M. Moore, 279–294, doi: 10.1142/9789811203787_0015

Baranec, C., Riddle, R., Law, N. M., et al. 2014, ApJL, 790, L8, doi: 10.1088/2041-8205/790/1/L8

Baranec, C., Chun, M., Hall, D., et al. 2018, in Society of Photo-Optical Instrumentation Engineers (SPIE) Conference Series, Vol. 10703, Adaptive Optics Systems VI, ed. L. M. Close, L. Schreiber, & D. Schmidt, 1070327, doi: 10.1117/12.2312835

Bellm, E. C., Kulkarni, S. R., Barlow, T., et al. 2019, PASP, 131, 068003, doi: 10.1088/1538-3873/ab0c2a

Blondin, S., & Tonry, J. L. 2007, ApJ, 666, 1024, doi: 10.1086/520494

Bohlin, R. C., Gordon, K. D., & Tremblay, P. E. 2014, PASP, 126, 711, doi: 10.1086/677655

Boone, K., Aldering, G., Copin, Y., et al. 2018, PASP, 130, 064504, doi: 10.1088/1538-3873/aab0fe

Bradley, L., Sipocz, B., Robitaille, T., et al. 2019, astropy/photutils: v0.6, v0.6, Zenodo, Zenodo, doi: 10.5281/zenodo.2533376

Burns, C., Hsiao, E., Suntzeff, N., et al. 2021, The Astronomer's Telegram, 14441, 1

Buton, C. 2009, Theses, Université Claude Bernard - Lyon I. https://tel.archives-ouvertes.fr/tel-00465853

Buton, C., Copin, Y., Aldering, G., et al. 2013, A&A, 549, A8, doi: 10.1051/0004-6361/201219834

Carnall, A. C. 2017, arXiv e-prints, arXiv:1705.05165. https://arxiv.org/abs/1705.05165

Chambers, K. C., Magnier, E. A., Metcalfe, N., et al. 2016, arXiv e-prints, arXiv:1612.05560. https://arxiv.org/abs/1612.05560

Coughlin, M. W. 2020, Nature Astronomy, 4, 550, doi: 10.1038/s41550-020-1130-3

Coulter, D. A., Foley, R. J., Kilpatrick, C. D., et al. 2017, Science, 358, 1556, doi: 10.1126/science.aap9811

Cuillandre, J. C., Magnier, E., Sabin, D., & Mahoney, B. 2016, in Astronomical Society of the Pacific Conference Series, Vol. 503, The Science of Calibration, ed. S. Deustua, S. Allam, D. Tucker, & J. A. Smith, 233

Cuillandre, J.-C., Magnier, E. A., Isani, S., et al. 2002, in Society of Photo-Optical Instrumentation Engineers (SPIE) Conference Series, Vol. 4844, Observatory Operations to Optimize Scientific Return III, ed. P. J. Quinn, 501–507, doi: 10.1117/12.460613

Da Silva Pereira, R. 2008, Theses, Université Paris-Diderot - Paris VII. https://tel.archives-ouvertes.fr/tel-00372504

de Jaeger, T., Shappee, B. J., Kochanek, C. S., et al. 2022, MNRAS, 509, 3427, doi: 10.1093/mnras/stab3141

Dimitriadis, G., Foley, R. J., Arendse, N., et al. 2022, ApJ, 927, 78, doi: 10.3847/1538-4357/ac4780

Dopita, M., Hart, J., McGregor, P., et al. 2007, Ap&SS, 310, 255, doi: 10.1007/s10509-007-9510-z

Filippenko, A. V. 1982, PASP, 94, 715, doi: 10.1086/131052

Foley, R. J., Challis, P. J., Chornock, R., et al. 2013, ApJ, 767, 57, doi: 10.1088/0004-637X/767/1/57

Foreman-Mackey, D., Hogg, D. W., Lang, D., & Goodman, J. 2013, PASP, 125, 306, doi: 10.1086/670067

Fraser, M., Stritzinger, M. D., Brennan, S. J., et al. 2021, arXiv e-prints, arXiv:2108.07278. https://arxiv.org/abs/2108.07278

Fremling, C., Miller, A. A., Sharma, Y., et al. 2020, ApJ, 895, 32, doi: 10.3847/1538-4357/ab8943

Gal-Yam, A., Bruch, R., Schulze, S., et al. 2022, Nature, 601, 201, doi: 10.1038/s41586-021-04155-1

Garrappa, S., Buson, S., Franckowiak, A., et al. 2019, ApJ, 880, 103, doi: 10.3847/1538-4357/ab2ada

[6] https://www.lsst.org/about/project-status

Hamuy, M., Maza, J., Phillips, M. M., et al. 1993, AJ, 106, 2392, doi: 10.1086/116811

Harris, C. R., Millman, K. J., van der Walt, S. J., et al. 2020, Nature, 585, 357, doi: 10.1038/s41586-020-2649-2

Hinkle, J. T., Holoien, T. W. S., Auchettl, K., et al. 2021a, MNRAS, 500, 1673, doi: 10.1093/mnras/staa3170

Hinkle, J. T., Holoien, T. W. S., Shappee, B. J., et al. 2021b, arXiv e-prints, arXiv:2108.03245. https://arxiv.org/abs/2108.03245

Hinkle, J. T., Tucker, M. A., Shappee, B. J., et al. 2022a, arXiv e-prints, arXiv:2202.05281. https://arxiv.org/abs/2202.05281

Hinkle, J. T., Kochanek, C. S., Shappee, B. J., et al. 2022b, arXiv e-prints, arXiv:2206.04071. https://arxiv.org/abs/2206.04071

Ho, A. Y. Q., Perley, D. A., Gal-Yam, A., et al. 2021, arXiv e-prints, arXiv:2105.08811. https://arxiv.org/abs/2105.08811

Hodapp, K. W., Denneau, L., Tucker, M., et al. 2020, AJ, 160, 164, doi: 10.3847/1538-3881/abad96

Holoien, T. W. S., Huber, M. E., Shappee, B. J., et al. 2019, ApJ, 880, 120, doi: 10.3847/1538-4357/ab2ae1

Holoien, T. W. S., Auchettl, K., Tucker, M. A., et al. 2020, ApJ, 898, 161, doi: 10.3847/1538-4357/ab9f3d

Hsiao, E. Y., Conley, A., Howell, D. A., et al. 2007, ApJ, 663, 1187, doi: 10.1086/518232

Hunter, J. D. 2007, Computing in Science and Engineering, 9, 90, doi: 10.1109/MCSE.2007.55

IceCube Collaboration, Aartsen, M. G., Ackermann, M., et al. 2018, Science, 361, eaat1378, doi: 10.1126/science.aat1378

Ivezić, Ž., Kahn, S. M., Tyson, J. A., et al. 2019, ApJ, 873, 111, doi: 10.3847/1538-4357/ab042c

Kausch, W., Noll, S., Smette, A., et al. 2015, A&A, 576, A78, doi: 10.1051/0004-6361/201423909

Kochanek, C. S., Shappee, B. J., Stanek, K. Z., et al. 2017, PASP, 129, 104502, doi: 10.1088/1538-3873/aa80d9

Kulkarni, S. R. 2020, arXiv e-prints, arXiv:2004.03511. https://arxiv.org/abs/2004.03511

Küsters, D., Lombardo, S., Kowalski, M., et al. 2016, in Society of Photo-Optical Instrumentation Engineers (SPIE) Conference Series, Vol. 9908, Ground-based and Airborne Instrumentation for Astronomy VI, ed. C. J. Evans, L. Simard, & H. Takami, 99084V, doi: 10.1117/12.2232902

Küsters, D., Bastian-Querner, B., Aldering, G., et al. 2020, in Society of Photo-Optical Instrumentation Engineers (SPIE) Conference Series, Vol. 11447, Society of Photo-Optical Instrumentation Engineers (SPIE) Conference Series, 1144771, doi: 10.1117/12.2561602

Lamman, C., Baranec, C., Berta-Thompson, Z. K., et al. 2020, AJ, 159, 139, doi: 10.3847/1538-3881/ab6ef1

Lang, D., Hogg, D. W., Mierle, K., Blanton, M., & Roweis, S. 2010, AJ, 139, 1782, doi: 10.1088/0004-6256/139/5/1782

Lantz, B., Aldering, G., Antilogus, P., et al. 2004, in Society of Photo-Optical Instrumentation Engineers (SPIE) Conference Series, Vol. 5249, Optical Design and Engineering, ed. L. Mazuray, P. J. Rogers, & R. Wartmann, 146–155, doi: 10.1117/12.512493

Li, W., Filippenko, A. V., Chornock, R., et al. 2003, PASP, 115, 453, doi: 10.1086/374200

Li, W. D., Filippenko, A. V., Treffers, R. R., et al. 2000, in American Institute of Physics Conference Series, Vol. 522, Cosmic Explosions: Tenth AstroPhysics Conference, ed. S. S. Holt & W. W. Zhang, 103–106, doi: 10.1063/1.1291702

Lombardo, S., Küsters, D., Kowalski, M., et al. 2017, A&A, 607, A113, doi: 10.1051/0004-6361/201731076

McCully, C., Crawford, S., Kovacs, G., et al. 2018, Astropy/Astroscrappy: V1.0.5 Zenodo Release, v1.0.5, Zenodo, Zenodo, doi: 10.5281/zenodo.1482019

Mishra, H. D., Dai, X., Chen, P., et al. 2021, ApJ, 913, 146, doi: 10.3847/1538-4357/abf63d

Necker, J., de Jaeger, T., Stein, R., et al. 2022, MNRAS, 516, 2455, doi: 10.1093/mnras/stac2261

Neustadt, J. M. M., Holoien, T. W. S., Kochanek, C. S., et al. 2020, MNRAS, 494, 2538, doi: 10.1093/mnras/staa859

Newville, M., Otten, R., Nelson, A., et al. 2021, lmfit/lmfit-py: 1.0.3, 1.0.3, Zenodo, Zenodo, doi: 10.5281/zenodo.5570790

Nicholl, M., Smartt, S. J., Jerkstrand, A., et al. 2014, MNRAS, 444, 2096, doi: 10.1093/mnras/stu1579

Pellegrino, C., Howell, D. A., Terreran, G., et al. 2022, arXiv e-prints, arXiv:2205.07894. https://arxiv.org/abs/2205.07894

Perley, D. A., Fremling, C., Sollerman, J., et al. 2020, ApJ, 904, 35, doi: 10.3847/1538-4357/abbd98

Prentice, S. J., Maguire, K., Smartt, S. J., et al. 2018, ApJL, 865, L3, doi: 10.3847/2041-8213/aadd90

Reback, J., jbrockmendel, McKinney, W., et al. 2022, pandas-dev/pandas: Pandas 1.4.2, v1.4.2, Zenodo, Zenodo, doi: 10.5281/zenodo.3509134

Reimann, H. G., Ossenkopf, V., & Beyersdorfer, S. 1992, A&A, 265, 360

Rubin, D., Aldering, G., Antilogus, P., et al. 2022, arXiv e-prints, arXiv:2205.01116. https://arxiv.org/abs/2205.01116

Salama, M., Ou, J., Baranec, C., et al. 2021, AJ, 162, 102, doi: 10.3847/1538-3881/ac0445

Shappee, B. J., Prieto, J. L., Grupe, D., et al. 2014, ApJ, 788, 48, doi: 10.1088/0004-637X/788/1/48

Shappee, B. J., Simon, J. D., Drout, M. R., et al. 2017, Science, 358, 1574, doi: 10.1126/science.aaq0186

Smartt, S. J., Valenti, S., Fraser, M., et al. 2015, A&A, 579, A40, doi: 10.1051/0004-6361/201425237

Smette, A., Sana, H., Noll, S., et al. 2015, A&A, 576, A77, doi: 10.1051/0004-6361/201423932

Steinbring, E., Cuillandre, J.-C., & Magnier, E. 2009, PASP, 121, 295, doi: 10.1086/597766

Tonry, J. L., Denneau, L., Heinze, A. N., et al. 2018a, PASP, 130, 064505, doi: 10.1088/1538-3873/aabadf

Tonry, J. L., Denneau, L., Flewelling, H., et al. 2018b, ApJ, 867, 105, doi: 10.3847/1538-4357/aae386

Trakhtenbrot, B., Arcavi, I., Ricci, C., et al. 2019, Nature Astronomy, 3, 242, doi: 10.1038/s41550-018-0661-3

Tucker, M. A., Huber, M., Shappee, B. J., et al. 2018a, The Astronomer's Telegram, 11473, 1

Tucker, M. A., Shappee, B. J., Holoien, T. W. S., et al. 2018b, ApJL, 867, L9, doi: 10.3847/2041-8213/aae88a

Valenti, S., Sand, D. J., Yang, S., et al. 2017, ApJL, 848, L24, doi: 10.3847/2041-8213/aa8edf

Virtanen, P., Gommers, R., Oliphant, T. E., et al. 2020, Nature Methods, 17, 261, doi: 10.1038/s41592-019-0686-2

Wood-Vasey, W. M., Aldering, G., Nugent, P., et al. 2002, IAUC, 7902, 3

Ziegler, C., Law, N. M., Baranec, C., et al. 2018, AJ, 156, 83, doi: 10.3847/1538-3881/aace59